Carbonate Stable Isotope Data Suggest Freshwater Environment for the McMurray Formation (Aptian), Alberta, Canada

Franek Hasiuk [1,*], Abdullah Wahbi [2,3], Luis González [2], Mike Blum [2] and Greg Ludvigson [1]

1 Kansas Geological Survey, University of Kansas, Lawrence, KS 66045, USA; gludvigson@ku.edu
2 Department of Geology, University of Kansas, Lawrence, KS 66045, USA; abdullah.wahbi.1@gmail.com (A.W.); luis.a.gonzalez@ku.edu (L.G.); mblum@ku.edu (M.B.)
3 Saudi Aramco, Dhahran 31311, Eastern Province, Saudi Arabia
* Correspondence: franek@ku.edu

Abstract: Stable isotope, trace element, and cathodoluminescence analyses were performed on gastropods and matrix from rock cores of the Middle to Upper McMurray Formation (Lower Cretaceous/Aptian, Northwestern Alberta, Canada) to characterize the extent to which pristine material remained from which depositional environmental conditions could be estimated. Aragonitic gastropod shells retain their original depositional chemistry, and along with other closely associated authigenic carbonate components, indicate that the Middle to Upper McMurray Formation was deposited in a freshwater environment that was part of a continent-scale river system.

1. Introduction

One of the most fundamental contributions to science that sedimentary geologists can make is the interpretation of a depositional environment from careful descriptions of sedimentary strata. These interpretations have such diverse and important implications as deciphering the movement of continents, the evolution of organisms, the waxing and waning of ice sheets, and the modeling of the distribution of economic resources. Despite this importance, interpretations of depositional environment are just that, *interpretations*, based on what can be no more than a "postage stamp" of all possible observations (e.g., how representative is a single drill core of an entire depositional environment?), using modern analogs (e.g., how representative is a modern reef of an ancient one?), or even the methods used (e.g., how might a depositional environment look different in seismic data versus outcrop versus well logs?). As one might imagine, such complications can lead to rather vociferous debate over the origins of a particular sedimentary stratum.

One such debate is related to the Lower Cretaceous McMurray Formation (Alberta, Canada), which hosts some of the world's largest hydrocarbon deposits in the form of bitumen-saturated sandstones in the Cold Lake, Athabasca, and Peace River Oil Sands Areas of east central Alberta (Figure 1A). These deposits, along with similarly sized bitumen deposits in Venezuela, represent ~70% of fluid hydrocarbons that have been discovered to date globally [1], and efficient resource extraction relies on accurate models of the deposits from which production is occurring. For bitumen deposits being open-pit mined, mine managers need to know which direction to continue excavating to produce maximum-grade ore. For bitumen deposits being produced by steam injection, drilling managers need to know where to place wells in the subsurface that maximizes the heating effect of the steam and maximizes the flow of liquid bitumen to collection wellbores. In both cases, knowledge of the depositional environment with its component facies, rock properties, pore types, and connectivity in the subsurface is essential for production performance prediction.
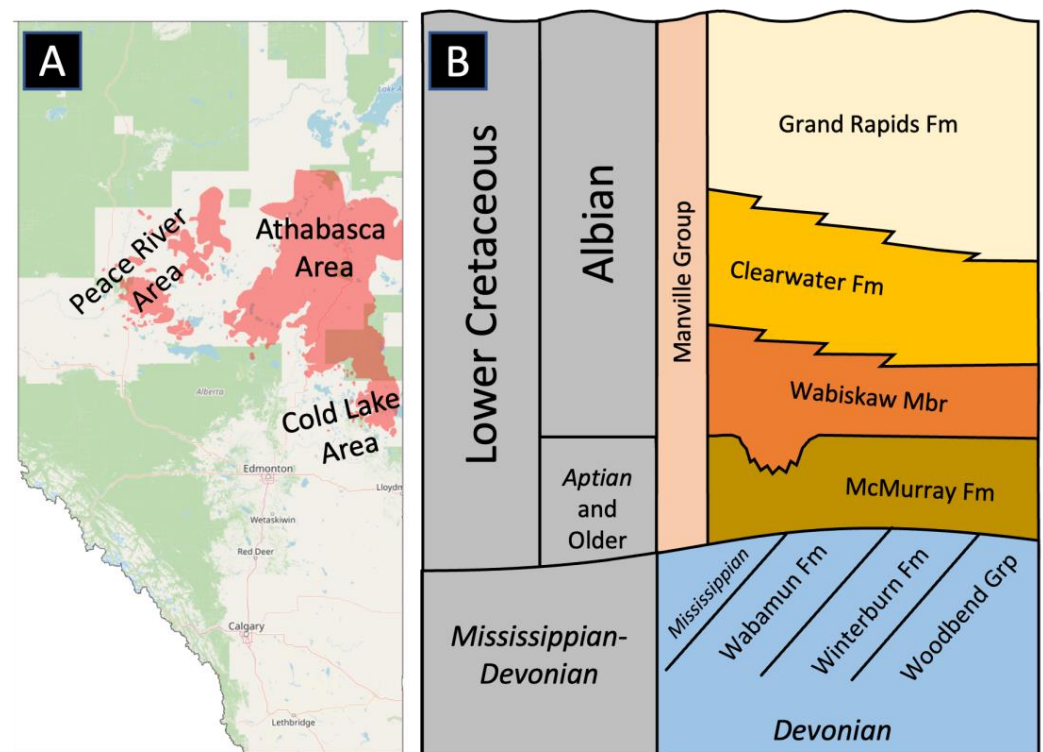
Figure 1. (**A**) Location map of the Aptian Ft McMurray Formation samples analyzed in this study [2]. (**B**) Regional stratigraphic column showing the context for the McMurray Formation (from [3]).

Despite this utility, there remains disagreement over such basic interpretations about the Middle to Upper McMurray Formation, such as whether it was deposited in a brackish estuarine environment with tidal influences or by a large fully freshwater fluvial system. For example, the estuarine model developed from a generation of studies of ichnofauna within McMurray sand bodies, which have been interpreted to represent brackish water-stressed environments typical of estuaries in the modern world. By contrast, the large river system point-of-view developed due to (a) similarities in plan-view geometries between McMurray sand bodies, as seen in 3D seismic data and large modern-day meandering river systems [4–8], and (b) studies of detrital zircon U-Pb ages distributions from McMurray channelbelt sandstones that define a continental-scale drainage area [9–12].

This debate has been referred to as the McMurray Conundrum (see [13,14]) because both interpretations are grounded on empirical data but are seemingly irreconcilable. Viewing the McMurray as part of a giant river system is not, in itself, inherently irreconcilable with brackish estuarine conditions inferred from the trace fossil record. However, rivers undergo inherent downstream morphological and sedimentary transformations as they flow through their hydraulic backwater reach, which is where rivers approach the shoreline and begin to feel the influence of the ocean on flow and sediment transport [12,15,16]. Rates of lateral migration and widths of channelbelt sands decrease significantly in the downstream direction, and channels become avulsive, with an overall distributive pattern. McMurray channelbelts and constituent point bars demonstrate a scale of lateral migration and amalgamation that is the norm upstream from the backwater reach and extends downstream to the tidal part of large modern rivers but has not been observed in the lowermost 100s of kilometers of large rivers where saltwater can penetrate during low flow periods [12].

This contribution reports on a direct test of the freshwater vs. brackish hypotheses by geochemically analyzing well-preserved carbonate material from fossil gastropods and co-occurring diagenetic carbonates recovered from what is interpreted to be abandoned channel fill facies in a McMurray core. Carbonate stable isotopes (i.e., $\delta^{18}O$, $\delta^{13}C$) are commonly used as proxies for paleoenvironmental conditions at the time of carbonate

mineral precipitation and are, therefore, often useful in interpreting paleoenvironments of deposition [17,18]. Interpretation of these data using empirically derived fractionation factors can even allow for quantitative estimates of both water temperature and carbon and oxygen isotopic systematics to be calculated [19].

Holmden et al. [20,21] carried out basin-scale evaluations of the marine to freshwater stable isotope paleohydrology of Early Cretaceous units of the Western Canada Sedimentary Basin. They integrated datasets on the δ^{18}O, δ^{13}C, and ^{87}Sr/^{86}Sr of well-preserved molluscan skeletal aragonite and associated authigenic carbonates to characterize isotopic ranges of marine, freshwater, and brackish depositional systems. They specified the δ^{18}O composition of -0.5‰ VSMOW for Early Cretaceous seawater. Using a specified paleolatitude of 60° N, they noted differences in freshwater compositions related to precipitation at lower (-4.5 to -12‰ VSMOW) and higher altitudes (-17.5 to -20‰ VSMOW), along with average basin river waters (-14 to -17‰ VSMOW).

Ufnar et al. [22] specified freshwater δ^{18}O compositions of -10.5 to -15.5‰ VSMOW based on analyses of paleosol siderites in northern British Columbia. Ufnar et al. [23] further noted a steepened latitudinal δ^{18}O gradient in the Cretaceous mid-latitudes to the Cretaceous polar regions with yet more depleted values at higher latitudes. Using an expanded pedogenic carbonate dataset, Suarez et al. [24] estimated Cretaceous lowland paleo-precipitation δ^{18}O values from 40° N to 60° N as ranging between about -8 and -16‰ VSMOW. More recently, Ross et al. [25] presented a revised meridional gradient incorporating new polar data from the Canadian Sverdrup Basin with estimated Cretaceous lowland paleo-precipitation δ^{18}O values from 40° N to 60° N ranging between -9 and -15‰ VSMOW.

Geologic Setting

During the time of deposition of the Lower Cretaceous McMurray Formation, Lower Manville Group, east–central Alberta, Canada, the Western Cordillera of North America was undergoing a period of complex tectonic activity involving arc magmatism, fold-and-thrust belt development, and foreland basin accumulation [26,27]. The episodic nature of these tectonic themes resulted in multiple episodes of deposition and erosion within the foreland basin beginning with the accumulation of the McMurray Formation [28].

The McMurray Formation has long been considered to be Aptian in age [29]. This interpretation is supported by new high-precision thermal ionization mass spectrometry (TIMS) detrital zircon U-Pb ages from isolated zircon grains [30,31], which show that McMurray Formation deposition included the period ca. 121–115 Ma, and by lower precision detrital zircon U-Pb maximum depositional ages from laser ablation inductively coupled mass spectrometry (LA-ICPMS) techniques, which place deposition from ca. 122–114 Ma [12]. Re-Os dates [32] are largely similar to these detrital zircon ages, suggesting nearly simultaneous oil migration into the McMurray Formation (the ultimate source of bitumen for the oil sands deposits) and may explain how these deposits have remained poorly lithified.

The McMurray rests on the sub-Cretaceous unconformity, which is regional to subcontinental in scale; within the Alberta Oil Sands Areas, the McMurray overlies Devonian carbonates of the Beaverhill Lake Group through the Wabamun Formation [33]. The unconformity has been interpreted to have been the result of the penecontemporaneous dissolution of evaporites within the underlying Devonian section during deposition of the Lower McMurray [34,35], though evidence of a sub-Cretaceous unconformity has broad/continental expression in North America with a north–south extent of over 1000 km at the base of the Zuni Supersequence [36]. The McMurray is overlain by the Wabiskaw Member of the Clearwater Formation (Upper Manville Group), which is from the Albian age [29] and has yielded detrital zircon U-Pb maximum depositional ages of ca. 113–111 Ma [12].

The division of the McMurray Formation Into lower, middle, and upper parts has been observed from some of its earliest investigations [37] . The lower consists of almost exclusively fluvial environments, the middle is dominantly fluvial with some evidence

of marine influence, and the upper represents marine shoreface deposition [38]. Earlier work interpreted the Lower McMurray as fluvial, the Middle McMurray as Gilbert-type deltas emptying into a lake or lagoon while noting a lack of marine fossils in the foreset beds [37,39], and the Upper McMurray as deposited into an estuary.

Nelson and Glaister [40] provided perhaps the first rigorous chronostratigraphic framework for the McMurray, identifying the three major units bounded by chronostratigraphic surfaces. Each unit was interpreted to record progradation to the modern-day southwest. A more recent synthesis stated that for the larger Wabiskaw–McMurray succession, "no clear distinctions can be made between the middle member estuarine and upper member coastal plain lithofacies associations" and "no single model applies to the total succession that is preserved" [33]. Putting the deposits in a sequence stratigraphic framework, that study found at least five parasequences, each preserving remnants of fluvial, estuarine, and bay-fill facies [33], with more parasequences preserved in areas of greater accommodation. More recent work has shown that the McMurray was composed of three systems draining a large area of the North American continent from as far as the Appalachians and southern Rocky Mountains [41].

Tidal bundles and mud couplets were used as evidence of subtidal estuarine conditions in the McMurray [42]. These features were used to estimate a spring tide range of 2 to 5 m, similar to the Westerschelde and Oosterschelde estuaries in the Netherlands and the Babahovo River Estuary in Ecuador [42]. Seismic geomorphology of specific oil sands deposits in the upper reaches of the Middle McMurray suggests that fluvial deposits were prevalent and were dominated by terrestrial palynomorphs yet still showed evidence of influence by marine processes [4].

Brackish-water fauna [43] were used to interpret a transgressive sequence in the upper member [44]. For example, the foraminifera *Ammodiscus* sp., *Haplophragmoides* cf. *H. sluzari*, *Haplophragmoides* sp., *Miliammina sproulei* var. *gigantea*, *Trochammina mcmurrayensis*, *Trochammina* sp., and *Verneuilinoides* sp. were recognized in the Upper McMurray [44]. Based on modern interpretations, while individual species from this assemblage might represent marine or brackish conditions, the presence of the complete assemblage would represent brackish conditions (Scott Ishman, pers. Communication, 2022). Trace fossils have also been used as evidence of brackish-to-marine depositional environments in these strata [13,14,45].

2. Methods

2.1. Sample Preparation

The one core sample used in this study came from well ID 1AA/06-07-093-07 W4/00 (Name: IMP OIL RES V M04 ASPEN 6-7-93-7. Field: 0998. TD 247.70 m. Drill date: 11 February 2016) (Figure 2). The specific sample analyzed consisted of a gastropod-rich coarse sandstone at a depth of 167.0 m in Core 3, Box 2, which showed variable bitumen saturation of open pore space.

Sawed (cut) core samples were digitally imaged prior to shipment for preparation of thin and thick counterpart sections (Spectrum Petrographics, Vancouver, WA, USA). At the preparation laboratory, samples were vacuum impregnated with blue-dyed epoxy resins to fill optically visible pore spaces in the rock. Counterpart samples were cut into thin micropolished sections (30 microns thickness) and thick sections (1 mm thickness). Thin sections were used for petrographic characterization under polarized light microscopy and cathodoluminescence (CL) imaging, and thick sections were imaged under paired reflected light and CL mapping to design the stable isotope microsampling campaign.
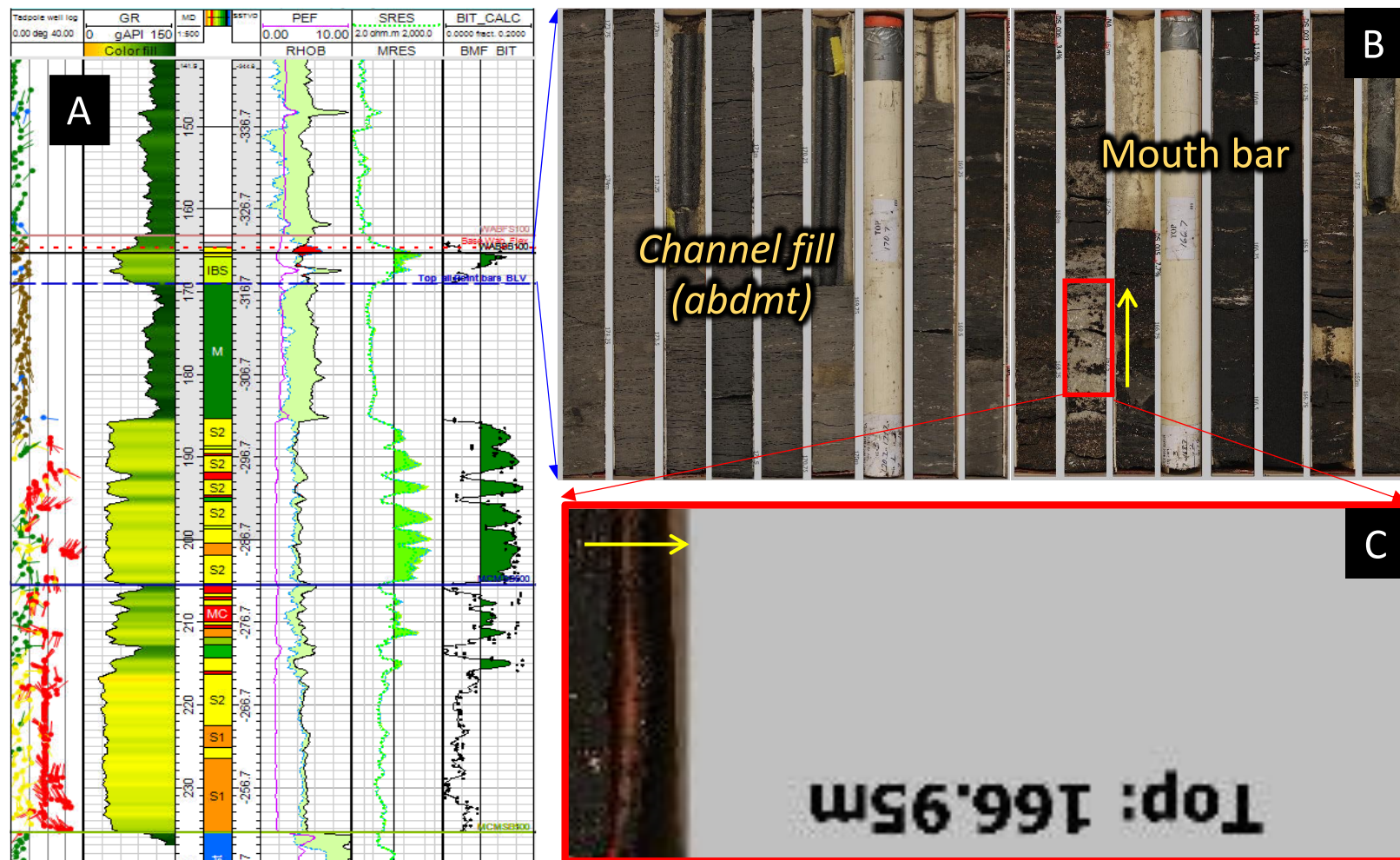
Figure 2. Geological context for samples analyzed in this study. (**A**) Well log suite from the cored well showing dipmeter (tadpole well log), gamma ray (GR), photoelectric (PEF), and shallow resistivity logs (SRES). Depth tracks show both measured depth from the top of the well (MD) and elevation with respect to sea level (SSTVD). (**B**) Core photos show the stratigraphic context for the interval sampled in this study. (**C**) The specific core interval from which gastropod samples were taken. Note bitumen saturation of the pore space. Yellow arrows indicate stratigraphic up.

2.2. Cathodoluminescence Imaging

Cathodoluminescence imaging (CL) was carried out in a Reliotron III cold cathode chamber (Relion Industries, Bedford, MA, USA) at the Digital Cathodoluminescence Imaging Laboratory (Kansas Geological Survey, Lawrence, Kansas) under operating conditions including a rarified helium atmosphere at 50 milliTorr, an accelerating voltage of 10 kV, and a beam current of 0.5 mA. Macroscopic imaging was carried out with a Canon SL1 16-megapixel DSLR camera with a macrolens suspended over the chamber with a boom stand, and microscopic imaging was carried out with an Olympus DP73 17-megapixel camera mounted on a modified Olympus BX41 microscope. Most mollusk shells were composed of their original depositional mineralogy, including aragonite, a $CaCO_3$ polymorph, which is highly susceptible to either dissolution or replacement by the mineral calcite in early diagenetic environments. To ensure that the shell materials from our samples retained their original chemistry from the depositional environment, the samples were subjected to cathodoluminescence imaging to check for the yellow-green luminescence characteristic of well-preserved shell aragonite.

2.3. Elemental Analysis

Elemental analysis was performed on a JEOL JXA-8230 Superprobe equipped with five wavelength-dispersive spectrometers (Department of Earth and Environmental Sciences, University of Iowa, Iowa City, IA, USA). Elemental maps of Fe and Ca concentrations were prepared by mapping spots on thin micropolished sections on a rectangular grid with 20 μm spacings. The analyses showed that all matrix carbonates are siderite ($FeCO_3$), while molluscan shell material and spar cement filling intrashell voids are $CaCO_3$.

2.4. Isotope Sampling

The collection of powders from thick micropolished sections was performed using a stereomicroscope-mounted microdrill assembly with 0.3 to 0.5 mm diameter carbide dental burrs. Samples were weighed to produce 50–100 μg of material for pure carbonates. More material was collected from impure material (e.g., siliciclastic matrix) to ensure enough signal would be generated during mass spectrometry.

2.5. Isotope Analysis

Samples were analyzed at the Keck-NSF Paleoenvironmental and Environmental Stable Isotope Laboratory (Department of Geology, University of Kansas, Lawrence, KS, USA). Approximately 100 μg of the sample was weighed into a stainless-steel boat using a Mettler Toledo microbalance. Stainless steel boats were placed in a brass convoy, and samples were vacuum roasted at 200 °C for 1 h to remove volatiles. Samples were analyzed, and sample CO_2 was generated by a reaction with 3 drops of 100% H_3PO_4 at 70 °C for 9 min using a Thermo Scientific Kiel IV Carbonate Device interfaced to the inlet of a Thermo MAT 253 dual-inlet mass spectrometer. Carbonate $\delta^{13}C$ and $\delta^{18}O$ isotope data are reported relative to VPDB. Precision was monitored through the daily analysis of NBS-18 and or NBS-19 and is better than 0.10‰ for both $\delta^{13}C$ and $\delta^{18}O$.

Reported siderite $\delta^{18}O$ values were corrected for acid fractionation using data from Carothers et al. (1988). Paleotemperature for the site was calculated using 54° N paleolatitude [46] and the latitudinal leaf physiognomy–temperature relationship [24] as follows:

$$t(°C) = 30.25 - 0.2025 \cdot Lat - 0.0006 \cdot Lat^2 \qquad (1)$$

The calculated mean annual temperature is 17.7 °C.

We calculated $\delta^{18}O_w$ for siderite and calcite, assuming that mineral precipitation occurred from groundwaters at the calculated mean annual temperature. Fractionation factors were calculated using the calcite-water fractionation factor from [47] and the siderite-water fractionation factor from [48]. We then used the calculated fractionation factors and the mineral $\delta^{18}O$ to calculate $\delta^{18}O_w$.

Unlike their counterparts in marine and hypersaline systems, freshwater mollusks secrete their $CaCO_3$ shells only at temperatures between 10 °C and ~38 °C [49]. Bulk freshwater molluscan aragonite $\delta^{18}O$ in this temperature range is correlated with mean river water $\delta^{18}O$ [49] and described by the following equation:

$$\delta^{18}O_{aragonite} = 0.89 \cdot \delta^{18}O_{water} - 0.98 \tag{2}$$

To calculate the temperature for bulk molluscan aragonite precipitation, we utilize the aragonite-water fractionation factor derived by [50] from data from [51] as follows:

$$1000ln\alpha_{aragonite-water} = 2.559 \cdot \frac{10^6}{T^2} + 0.715 \tag{3}$$

We use the fractionation factors from [52] to calculate the $\delta^{13}C$ of HCO_3^-. For calcite, we use the calcite-HCO_3^- fractionation factor from [52] as follows:

$$1000ln\alpha_{calcite-HCO_3^-} = 0.095 \cdot \frac{10^6}{T^2} + 0.91 \tag{4}$$

For siderite and aragonite, there are only published fractionation factors for mineral-CO_2. For siderite, we utilize the fractionation factor of [53] as follows:

$$1000ln\alpha_{siderite-CO_2} = 0.861 \cdot \frac{10^6}{T^2} + 0.82 \tag{5}$$

We derived an aragonite–CO_2 fractionation relationship from the data presented by [51] as follows:

$$1000ln\alpha_{aragonite-CO_2} = 1.68 \cdot \frac{10^6}{T^2} - 8.47 \tag{6}$$

We use Deines et al.'s [52] $HC—CO_2$ fractionation factor and siderite and aragonite $\delta^{13}C$ of CO_2 to calculate $\delta^{13}C$ of HCO_3^-.

3. Results

3.1. Petrographic and Cathodoluminescence Imaging

Samples of carbonate concretions all have a fine-grained sandstone matrix, and gastropod shells in samples 2 and 3 showed extensive evidence of aragonite dissolution within their nacreous layer, which is now filled with vacuum-injected, blue-dyed epoxy resin. By contrast, the aragonitic nacreous layers in gastropod shells in sample 1 showed no evidence of dissolution, with full preservation of the gastropod shell. Under cross-polarized light, the nacreous layers displayed the "zebra striping" pattern indicative of a crossed-lamellar structure that is characteristic of aragonitic gastropod shells ([54]; pp. 154–156). Where cross-section views of whole shell morphology are visible, the gastropods display high-spired morphologies (Figure 3), although insufficient morphological and surface textural information was available to make more detailed taxonomic (and thence paleoenvironmental) interpretations. Preservation quality was likely at least partially a result of the bitumen saturating in much of the larger open pore space in adjacent beds (Figure 1).

Some gastropod shells are filled with the surrounding sandstone matrix, but others are partly filled with geopetal muds overlain by carbonate cement (Figures 3–5). Wavelength-dispersive elemental mapping with an electron microprobe confirms that the gastropod shells and carbonate cement overlying the geopetal sediment fills are calcium carbonate ($CaCO_3$; Figure 3B). Elemental mapping also shows that the carbonate cement filling intergranular pores in the sandstone matrix and those pervading the geopetal sediments in the shells are siderite ($FeCO_3$; Figure 3C).
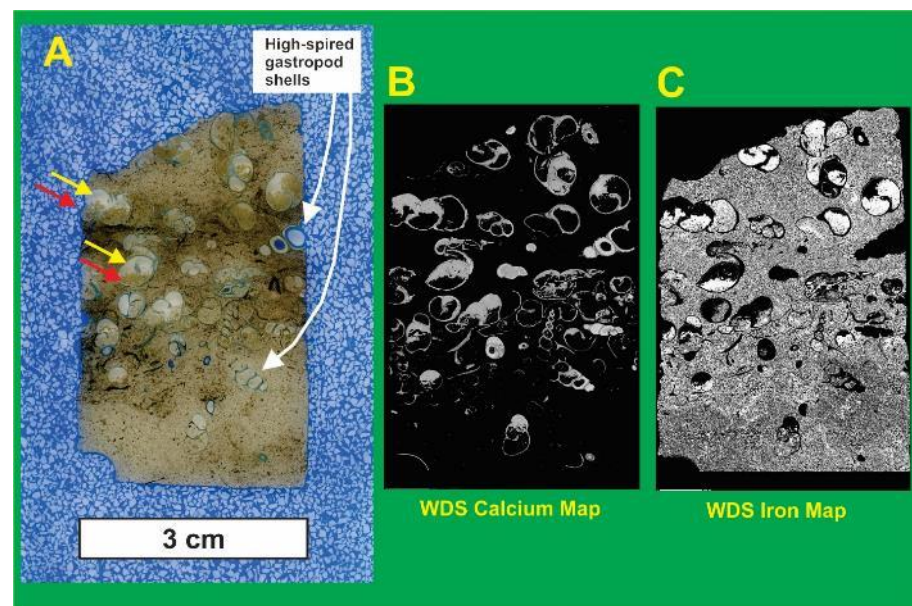
Figure 3. Images of the thin micropolished section in sample 1. Images are at the same scale and in the same orientation. (**A**) Flatbed-scanned color image of the thin section under reflected light. The high-spired morphology of gastropod shells (white arrows and in other positions) is apparent. The slab sample was immersed in feldspar sand while undergoing vacuum impregnation with blue-dyed epoxy resin, and those angular feldspar sand grains (white) are engulfed by the surrounding, blue-dyed resin. Two gastropod shells are highlighted with geopetal mud floors (red arrows) overlain by carbonate cement (yellow arrows). (**B**) Wavelength Dispersive Spectrometer (WDS) microprobe elemental map of calcium carbonate shown in white against black background. This image confirms the $CaCO_3$ composition of aragonitic gastropod shells and calcite cement overlying the geopetal sediment floors. (**C**) WDS microprobe elemental map of iron carbonate shown in white against black background. This image confirms the $FeCO_3$ composition of siderite cement pervading the geopetal muds filling gastropod shells and the siderite cement filling intergranular pores (white) between rigid silicate framework grains (black).
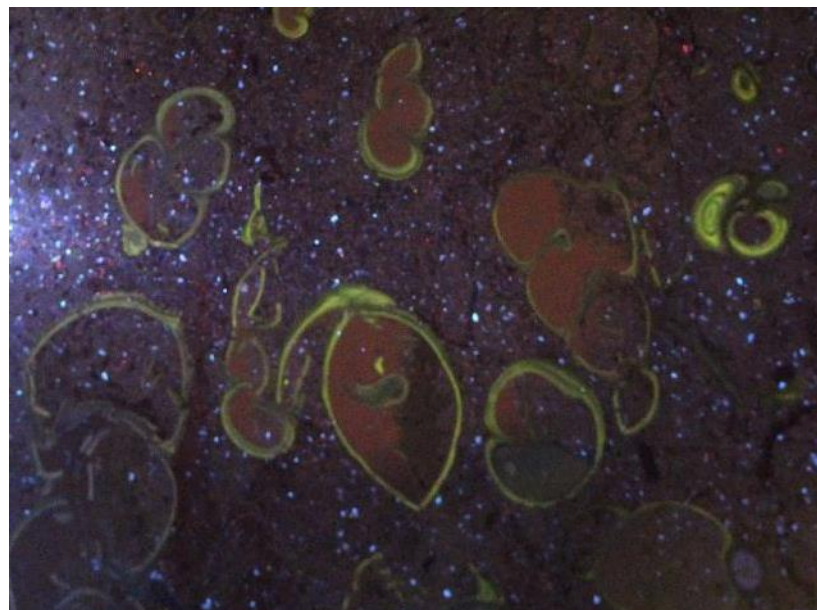

Figure 4. Cathodoluminescence macro photo of yellow-green luminescing gastropod shells in a siderite concretion from the Cretaceous McMurray Formation. The field of view is approximately 3 cm wide.

Cathodoluminescence (CL) imaging in sample 1's thin section shows that the gastropod nacreous layers all have a yellow-green luminescence color (Figures 4 and 5A), a characteristic of well-preserved molluscan aragonite [55–57]. CL imaging further showed that all the carbonate cement in the sample is non-luminescent (Figure 5B). Iron quenching of manganese-activated CL luminescence is a characteristic of sedimentary siderites as it is in calcite [58,59]. This was apparent in the siderite cement filling intergranular pores in the sandstone matrix and the siderite cement pervading the geopetal muds within the gastropod shells (Figure 5B). Calcite cement overlying the geopetal muds displayed non-luminescence (Figure 5B).

Petrographic imaging of sample 1's thin section shows that non-luminescent siderite cement in the sandstone matrix fills approximately 35 to 40% of the intergranular volume, an observation that has important implications for the timing of concretion formation. Intergranular volumes in this range are indicative of shallow burial depths preceding significant sediment compaction [60]. Enclosure of the delicate thin-shelled gastropod shells in the rigid framework of the siderite concretion precluded any deformation by compaction during later burial. Moreover, backscattered electron (BSE) imaging of the gastropod shells in sample 1 at the scanning electron microscope (SEM) scale shows that micron-scale lath-shaped siderite crystals contiguous with the pore-filling siderite cement penetrate the margins of the gastropod shells. This indicates that authigenic siderite cementation during concretion formation sealed the shell aragonite from dissolution by interaction with any later fluids.
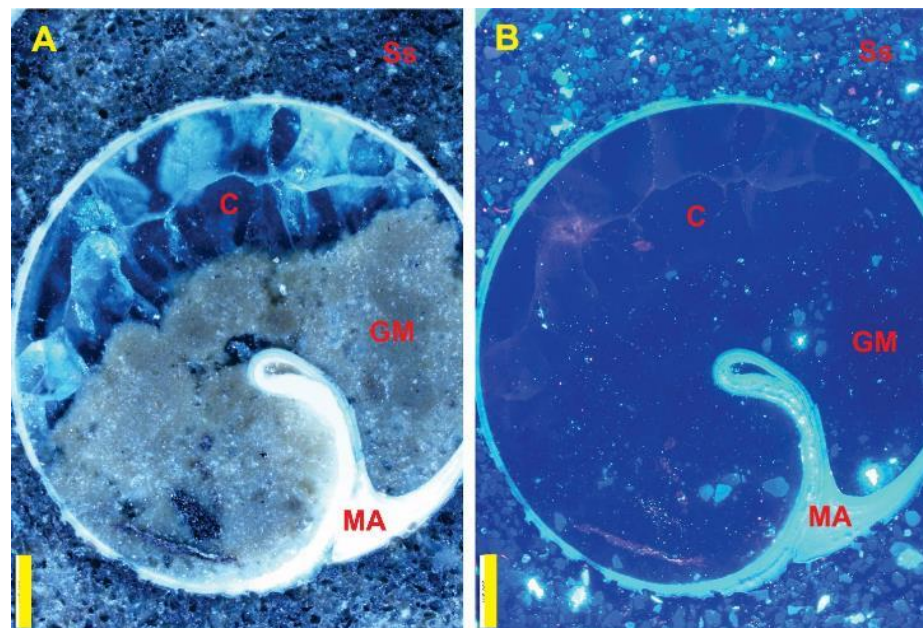

Figure 5. Paired reflected light and cathodoluminescence photomicrographs of the thick micropolished section in sample 1. Yellow scale bars are 500 microns in length. (**A**) Reflected light image. The nacreous layer of molluscan aragonite (MA) is highly reflective and appears bright white. The geopetal mud (GM) pervaded by microcrystalline siderite cement appears dark brown, except for reflective white silicate sand grains contained within. (**B**) Cathodoluminescence (CL) image. The uniform bright yellow-green CL luminescence of the molluscan aragonite (MA) confirms that the nacreous layers of the gastropod shells in sample 1 are pristine and thus likely retain their original geochemical compositions. Note the uniform non-luminescence of siderite cement pervading the geopetal mud (GM) and the siderite cement filling intergranular pores in the sandstone matrix (Ss). Framework silicate sand grains have a bright to faint blue CL luminescence [61].

3.2. Isotopic Data

All stable isotope data are reported with respect to the VPDB standard (Table 1). The isotopic data for each mineral component plots on distinct fields, although there are some minor overlaps of the siderite data with the calcite and aragonite data (Figure 6). Aragonite data fell between −8 and −12‰ δ^{18}O and +2 and +7‰ δ^{13}C. Calcite data plotted between −13 and −17‰ δ^{18}O and +15 and +18‰ δ^{13}C. Corrected siderite spanned between −7 and −13‰ δ^{18}O and +3 and +15‰ δ^{13}C. Two visually distinct trends can be recognized from the siderite data extending to more negative δ^{18}O and more positive δ^{13}C from an origin near −7‰ δ^{18}O and +3‰ δ^{13}C. The *siderite upper trend* tends toward but does not overlap with the calcite field. The *siderite lower trend* trends toward and ends with a significant overlap with the aragonite field.

Table 1. Stable isotope data.

Mass (mg)	ID1	Material	Note	Mineralogy	δ^{18}O (‰VPDB)	δ^{18}O (±1SD)	δ^{13}C (‰VPDB)	δ^{13}C (±1SD)
0.3857	MB-S1-26A	SAND	DARK	S	−6.39	0.01	3.76	0.01
0.3786	MB-S1-12B	SAND	DARK	S	−6.23	0.02	3.45	0.01
0.3943	MB-S1-24A	SAND	DARK	S	−5.89	0.02	3.14	0.01
0.3965	MB-S1-20C	SAND	DARK	S	−6.24	0.01	3.97	0.00
0.3977	MB-S1-27A	SAND	DARK	S	−6.26	0.02	3.98	0.01
0.3597	MB-S1-14A	SAND	DARK-CL	S	−6.68	0.02	4.17	0.01
0.3659	MB-S1-25A	SAND	LIGHT	S	−7.15	0.02	8.55	0.01
0.3799	MB-S1-17A	SAND	LIGHT	S	−6.60	0.02	5.41	0.01
0.3387	MB-S1-16B	SAND	LIGHT	S	−9.24	0.02	10.86	0.01
0.4097	MB-S1-11D	SAND	LIGHT	S	−6.80	0.01	7.26	0.00
0.3055	MB-S1-07B	SAND	LIGHT	S	−9.34	0.02	9.38	0.01
0.4228	MB-S1-09B	SAND	LIGHT	S	−8.79	0.03	6.28	0.00
0.3961	MB-S1-10C	SAND	LIGHT	S	−9.87	0.02	7.16	0.02
0.3192	MB-S1-31A	SAND	LIGHT	S	−7.51	0.03	7.61	0.01
0.5132	MB-S1-01E	SAND	SPAR	S	−6.41	0.01	7.26	0.01
0.4737	MB-S1-04E	SAND	SPAR	S	−10.04	0.03	6.63	0.01
0.354	MB-S1-13B	SAND	SPAR	S	−8.23	0.03	5.77	0.00
0.3711	MB-S1-14C	SAND	SPAR	S	−6.60	0.01	6.40	0.01
0.2047	MB-S1-05A	SAND	-	S	−6.38	0.02	5.80	0.01
0.24	MB-S1-15C	SAND	-	S	−8.63	0.01	10.19	0.01
0.2747	MB-S1-18B	SAND	-	S	−11.99	0.02	14.48	0.01
0.2034	MB-S1-03B	SAND	-	S	−11.25	0.02	13.36	0.01
0.2385	MB-S1-19D	SAND	-	S	−9.70	0.02	10.31	0.01
0.2141	MB-S1-06A	SAND	-	S	−7.09	0.01	6.12	0.01
0.3953	MB-S1-08A	SAND	-	S	−7.04	0.01	5.85	0.01
0.0588	MB-S1-7A	SHELL	BROWN	A	−10.38	0.01	4.11	0.01
0.1076	MB-S1-14b	SHELL	BROWN-EPOXY	A	−10.94	0.01	5.65	0.01
0.0923	MB-S1-13A	SHELL	DIRTY	A	−11.25	0.02	7.39	0.00
0.0587	MB-S1-11B	SHELL	WHITE	A	−8.80	0.01	3.76	0.02
0.0992	MB-S1-11C	SHELL	WHITE	A	−10.81	0.01	6.89	0.01
0.0856	MB-S1-18A	SHELL	WHITE	A	−11.16	0.02	5.07	0.01
0.0652	MB-S1-03C	SHELL	WHITE	A	−10.57	0.02	4.39	0.01
0.1003	MB-S1-03d	SHELL	WHITE	A	−10.64	0.02	5.86	0.02
0.2757	MB-S1-03e	SHELL	WHITE	A	-	-	-	-
0.0941	MB-S1-28a	SHELL	WHITE	A	−11.35	0.01	3.95	0.01
0.0789	MB-S1-05b	SHELL	WHITE	A	−12.27	0.02	9.73	0.02
0.0667	MB-S1-15d	SHELL	WHITE	A	−9.99	0.03	3.66	0.01
0.0876	MB-S1-11E	SHELL	WHITE	A	−10.21	0.03	4.44	0.01
0.0916	MB-S1-04C	SHELL	WHITE	A	−10.43	0.01	6.42	0.01
0.0909	MB-S1-23B	SHELL	WHITE	A	−11.69	0.01	6.39	0.01
0.0672	MB-S1-29A	SHELL	WHITE	A	−11.20	0.03	7.09	0.01
0.0817	MB-S1-15E	SHELL	WHITE	A	−9.89	0.02	4.11	0.01

Table 1. *Cont.*

Mass (mg)	ID1	Material	Note	Mineralogy	$\delta^{18}O$ (‰VPDB)	$\delta^{18}O$ ($\pm$1SD)	$\delta^{13}C$ (‰VPDB)	$\delta^{13}C$ ($\pm$1SD)
0.0863	MB-S1-11F	SHELL	WHITE	A	−9.75	0.01	3.72	0.01
0.0698	MB-S1-11G	SHELL	WHITE	A	−9.72	0.01	2.60	0.01
0.0732	MB-S1-04D	SHELL	WHITE	A	−11.32	0.02	6.22	0.01
0.4848	MB-S1-15A	SHELL	-	A	−10.15	0.01	4.78	0.01
0.1085	MB-S1-15B	SHELL	-	A	−16.36	0.02	1.11	0.01
0.0554	MB-S1-01A	SHELL	-	A	−10.02	0.01	3.78	0.00
0.0701	MB-S1-01B	SHELL	-	A	−9.56	0.01	3.31	0.01
0.0684	MB-S1-01C	SHELL	-	A	−9.53	0.01	4.79	0.01
0.094	MB-S1-03A	SHELL	-	A	−10.07	0.01	5.32	0.01
0.0571	MB-S1-09A	SHELL	-	A	−9.63	0.01	4.35	0.01
0.0971	MB-S1-04B	SHELL	-	A	−10.76	0.01	5.79	0.01
0.0794	MB-S1-12A	SHELL	-	A	−10.65	0.01	5.73	0.01
0.0659	MB-S1-16A	SHELL	-	A	−10.20	0.02	5.76	0.01
0.0547	MB-S1-21A	SHELL	-	A	−11.07	0.01	6.40	0.00
0.0833	MB-S1-22A	SHELL	-	A	−9.83	0.01	2.02	0.01
0.0892	MB-S1-23A	SHELL	-	A	−9.83	0.01	4.55	0.01
0.0791	MB-S1-02A	SPAR	CL	C	−14.48	0.01	17.27	0.01
0.1094	MB-S1-10B	SPAR	CL	C	−14.67	0.01	17.11	0.01
0.0877	MB-S1-02B	SPAR	CL	C	−14.61	0.01	17.42	0.01
0.0861	MB-S1-02C	SPAR	CL	C	−14.56	0.02	17.37	0.02
0.1712	MB-S1-19C	SPAR	DIRTY	C	−12.31	0.02	12.96	0.00
0.0705	MB-S1-01D	SPAR	NL	C	−14.56	0.01	17.31	0.01
0.0714	MB-S1-20A	SPAR	NL	C	−16.23	0.02	15.78	0.01
0.0715	MB-S1-20B	SPAR	NL	C	−16.18	0.02	15.48	0.01
0.0768	MB-S1-10A	SPAR	NL	C	−14.70	0.02	17.05	0.02
0.0934	MB-S1-19A	SPAR	NL	C	−16.24	0.01	15.67	0.01
0.1034	MB-S1-19B	SPAR	NL	C	−16.26	0.02	15.63	0.02
0.0542	MB-S1-04A	SPAR	NL	C	−14.61	0.02	17.30	0.01
0.0721	MB-S1-10D	SPAR	NL	C	−14.69	0.01	17.22	0.01
0.0835	MB-S1-20D	SPAR	NL	C	−16.26	0.01	15.89	0.01
0.0579	MB-S1-20E	SPAR	NL	C	−16.33	0.05	15.62	0.01
0.0795	MB-S1-17B	SPAR	NL	C	−15.16	0.01	16.19	0.01
0.0618	MB-S1-19E	SPAR	NL	C	−16.23	0.01	15.75	0.01
0.0733	MB-S1-02D	SPAR	NL	C	−14.52	0.01	17.10	0.00
0.0862	MB-S1-20F	SPAR	NL	C	−16.24	0.01	15.89	0.01
0.0961	MB-S1-03F	SPAR	NL	C	−14.02	0.02	15.95	0.01
0.0716	MB-S1-11A	SPAR	-	C	−14.51	0.03	17.07	0.00
0.0022	MB-S1-30A	SPAR	-	C	−12.32	0.03	8.57	0.00
0.0888	MB-S3-1	SHELL	NONPOROUS	A	−10.28	0.01	5.85	0.01
0.0531	MB-S3-2	SHELL	NONPOROUS	A	−10.42	0.04	5.77	0.01
0.0558	MB-S3-3	SHELL	NONPOROUS	A	−10.49	0.01	4.92	0.01
0.0645	MB-S3-4	SHELL	NONPOROUS	A	−9.48	0.02	5.92	0.01
0.0845	MB-S3-5	SHELL	NONPOROUS	A	−10.41	0.02	5.63	0.02
0.0723	MB-S3-6	SHELL	NONPOROUS	A	−9.92	0.02	6.03	0.01
0.0646	MB-S3-7	SHELL	NONPOROUS	A	−9.85	0.01	5.92	0.00
0.0755	MB-S3-8	SHELL	NONPOROUS	A	−9.95	0.02	6.03	0.01
0.092	MB-S3-9	SHELL	NONPOROUS	A	−9.83	0.01	5.96	0.01
0.0686	MB-S3-10	SHELL	NONPOROUS	A	−10.20	0.01	6.68	0.01
0.0559	MB-S3-11	SHELL	NONPOROUS	A	−10.71	0.01	4.54	0.01
0.0565	MB-S3-12	SHELL	NONPOROUS	A	−10.46	0.03	6.11	0.01
0.0909	MB-S3-13	SHELL	NONPOROUS	A	−8.83	0.01	6.37	0.01
0.0723	MB-S3-14	SHELL	NONPOROUS	A	−10.98	0.01	5.36	0.02
0.0874	MB-S3-15	SHELL	NONPOROUS	A	−9.62	0.01	6.24	0.01
0.0588	MB-S3-16	SHELL	NONPOROUS	A	−9.66	0.01	5.65	0.02
0.0576	MB-S3-17	SHELL	NONPOROUS	A	−8.92	0.01	7.13	0.01
0.0874	MB-S3-18	SHELL	NONPOROUS	A	−10.70	0.02	5.58	0.01

Table 1. *Cont.*

| Mass (mg)	ID1	Material	Note	Mineralogy	$\delta^{18}O$ (‰VPDB)	$\delta^{18}O$ ($\pm$1SD)	$\delta^{13}C$ (‰VPDB)	$\delta^{13}C$ ($\pm$1SD)
0.0874	MB-S3-19	SHELL	NONPOROUS	A	−6.02	0.03	1.24	0.01
0.0699	MB-S3-20	SHELL	NONPOROUS	A	−9.52	0.02	5.97	0.01
0.0629	MB-S3-21	SHELL	NONPOROUS	A	−9.56	0.04	5.83	0.04
0.0834	MB-S3-32	SHELL	NONPOROUS	A	−9.64	0.02	5.85	0.01
0.0632	MB-S3-34	SHELL	NONPOROUS	A	−10.15	0.02	5.89	0.01
0.0745	MB-S3-39	SHELL	NONPOROUS	A	−10.49	0.01	5.78	0.01
0.0622	MB-S3-40	SHELL	NONPOROUS	A	−10.34	0.02	5.64	0.01
0.0815	MB-S3-22	SHELL	POROUS	A	−9.57	0.01	6.18	0.00
0.1614	MB-S3-23	SHELL	POROUS	A	−9.48	0.01	6.90	0.01
0.1365	MB-S3-24	SHELL	POROUS	A	−8.75	0.01	6.31	0.00
0.1196	MB-S3-25	SHELL	POROUS	A	−9.66	0.01	5.86	0.01
0.1139	MB-S3-26	SHELL	POROUS	A	−9.92	0.01	5.93	0.01
0.1607	MB-S3-27	SHELL	POROUS	A	−9.42	0.02	7.00	0.01
0.125	MB-S3-28	SHELL	POROUS	A	−9.88	0.01	5.97	0.01
0.1548	MB-S3-29	SHELL	POROUS	A	−9.27	0.01	6.19	0.01
0.1429	MB-S3-30	SHELL	POROUS	A	−9.77	0.01	6.29	0.00
0.1125	MB-S3-31	SHELL	POROUS	A	−9.69	0.01	5.75	0.01
0.1755	MB-S3-33	SHELL	POROUS	A	−9.10	0.02	6.29	0.00
0.1877	MB-S3-35	SHELL	POROUS	A	−9.40	0.01	6.24	0.01
0.1373	MB-S3-36	SHELL	POROUS	A	−9.64	0.01	5.86	0.01
0.0647	MB-S3-37	SHELL	POROUS	A	−10.55	0.02	6.07	0.01
0.1211	MB-S3-38	SHELL	POROUS	A	−10.69	0.02	5.54	0.01
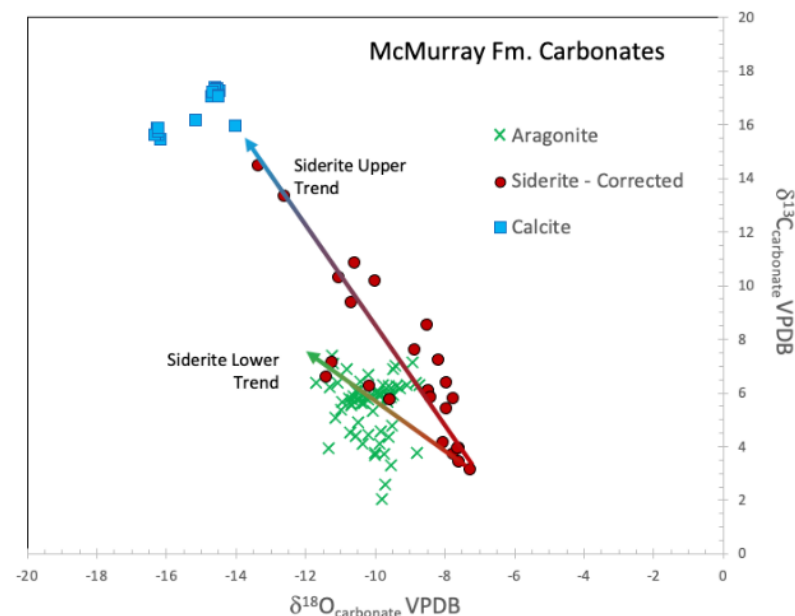
Figure 6. Plot of carbonate $\delta^{13}C$ vs. carbonate $\delta^{18}O$ showing clearly defined domains for sample phases (siderite matrix—red circles, aragonite gastropod shell material—green x's, calcite spar—blue squares). Two linear trends are suggestive of the mixing of a siderite endmember and aragonite/calcite endmembers.

4. Discussion

4.1. Stable Isotopic Paleohydrologic Calculations

Summary statistics for water (river- and groundwater) compositions are shown in Table 2 and plotted in Figure 7. The water $\delta^{18}O$ and $\delta^{13}C_{HCO_3^-}$ values calculated for each mineral define distinct fields. As expected, the siderite groundwater $\delta^{18}O$ and $\delta^{13}C_{HCO_3^-}$ values are highly variable. The siderite groundwater data overlap the aragonite-calculated

river water and calcite groundwater data. The siderite groundwater $\delta^{18}O$ and $\delta^{13}C_{HCO_3^-}$ have a small but significant overlap with the calcite groundwater field. The heavy endmembers of the aragonite river water and siderite groundwater $\delta^{18}O$ values have significant overlap (siderite -8.15‰ vs. aragonite -8.73‰), and average values are nearly identical (siderite -10.16‰ vs. aragonite -10.24‰). However, siderite-derived water $\delta^{13}C_{HCO_3^-}$ has only minor overlap with aragonite-derived water $\delta^{13}C_{HCO_3^-}$.

Table 2. Statistical summary of calculated river water temperature and isotopic compositions of river water and groundwater. $\delta^{18}O$ is in ‰ VSMOW. $\delta^{13}C$ is in ‰ VPDB.

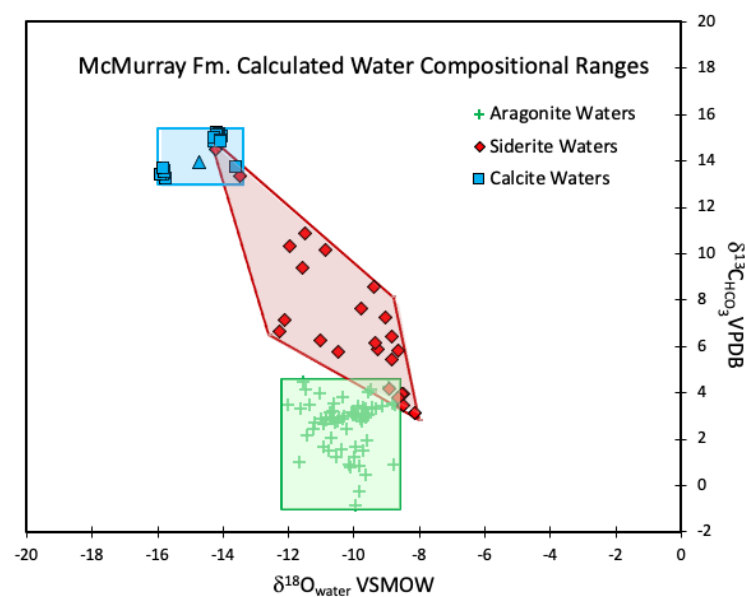|	Aragonite (River Water)			Calcite (Groundwater)		Siderite (Groundwater)	
	$\delta^{18}O_w$	t °C	$\delta^{13}C_{HCO_3^-}$	$\delta^{18}O_w$	$\delta^{13}C_{HCO_3^-}$	$\delta^{18}O_w$	$\delta^{13}C_{HCO_3^-}$
Max	-8.73	20.35	4.41	-13.59	15.20	-8.15	14.48
Min	-12.03	18.55	-0.94	-15.89	13.26	-14.22	3.14
Mean	-10.24	19.52	2.56	-14.82	14.29	-10.16	7.08
Std Dev	0.74	0.41	1.08	0.85	0.75	1.74	3.05
Range	3.30	1.80	5.35	2.30	1.94	6.07	11.34
+2 s	-8.38	20.54	5.26	-12.68	16.17	-5.82	14.70
-2 s	-12.10	18.51	-0.13	-16.96	12.40	-14.51	-0.54

Figure 7. Calculated $\delta^{18}O_w$ and $\delta^{13}C_{HCO_3^-}$ for waters that precipitated calcite, siderite, and aragonite phases analyzed in this study.

Mixing model/calculations (Figure 8) suggest that the siderite that defines the upper trend (Figure 6) precipitated from mixtures with no more than 80% contribution from the calcite-precipitating waters. The lower siderite data trend (Figure 6) appears to consist of two clusters. The heavier $\delta^{18}O$ and lower $\delta^{13}C$ siderite cluster is produced by mixtures containing less than 20% river waters. The cluster with lighter $\delta^{18}O$ and heavier $\delta^{13}C$, which entirely overlaps the aragonite data, appears to form from water mixtures that contain 95% to 50% river water.

In brief, the stable isotope compositions of mollusk shell aragonite and siderite matrix carbonates from the McMurray Formation core samples are characteristic of other freshwater paleoenvironments that have been sampled from early Cretaceous authigenic carbonates of northern Alberta [20,21], British Columbia [22], northern Alaska [62,63], and the Sverdrup Basin of the Canadian Arctic Archipelago [25]. The shell $\delta^{18}O$ values of about -10‰ ± 2‰ definitively rule out the involvement of marine fluids and are very similar to

other published and unpublished results from early Cretaceous terrestrial units from North America at paleolatitudes around 50° N. We do not see gastropod aragonite with $\delta^{18}O$ values that would be expected for marine aragonite in the Cretaceous age. Our aragonite is −8‰ $\delta^{18}O$ at its most positive. Even accounting for the 4‰ range in modern abiotic aragonite [64], we cannot reach the approximately −2‰ $\delta^{18}O$ that would be expected if precipitating from the global Cretaceous ocean [65].
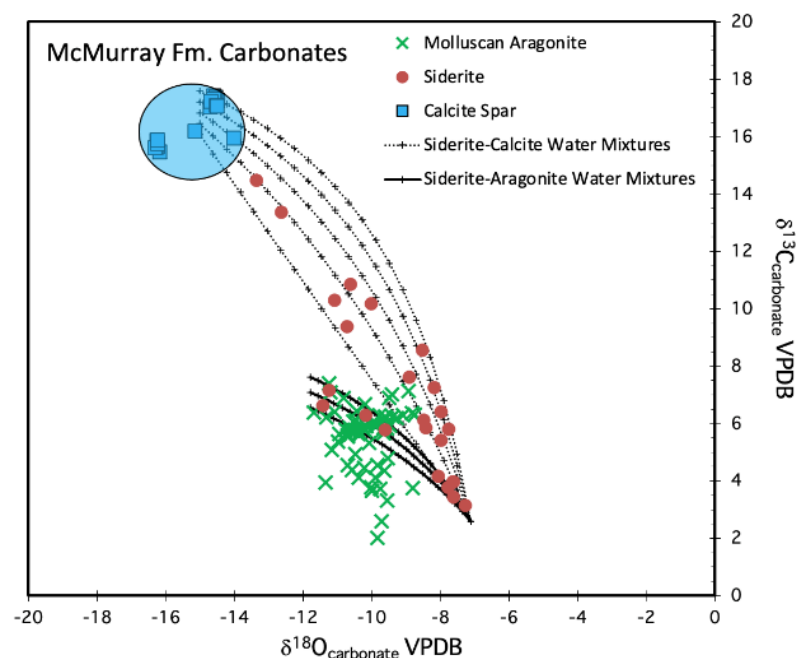
Figure 8. Mixing lines between siderite and calcite precipitating groundwaters, siderite precipitating groundwater, and river water.

The presence of well-preserved aragonite also argues against a normal marine depositional or diagenetic environment. In the modern period, aragonite is commonly observed to stabilize to calcite on the order of thousands of years [66].

All carbonates sampled from this study produced positive $\delta^{13}C$ values, ranging from about +1 to +17‰, which are also characteristic of high-latitude, early Cretaceous meteoric groundwater paleoenvironments [25,62,63]. This phenomenon has not yet been extensively explored in the published literature but is thought to have resulted from strongly methanogenic aquatic and paleo-groundwater environments in the Cretaceous greenhouse world.

Both the shell carbonates and their surrounding authigenic carbonates produced data that are arrayed along similarly shaped hyperbolic trends matching the highest $\delta^{18}O$ values with the lowest $\delta^{13}C$ values, and vice versa. The most parsimonious interpretation of these data is that both shell growth and authigenic cementation were influenced by fluid mixtures derived from locally infiltrated paleo-groundwater recharge (higher $\delta^{18}O$ values and lower $\delta^{13}C$ values) and regionally discharging paleo-groundwaters from a continental-scale flow system (lower $\delta^{18}O$ values and higher $\delta^{13}C$ values) that drained Laurentia. River water $\delta^{18}O$ is known to be controlled by the $\delta^{18}O$ of precipitation from upstream sources (and thus at higher elevations) through the so-called "catchment effect" [67]. In this way, river water may have a $\delta^{18}O$ more negative than expected from the elevation it was collected at. The $\delta^{18}O$ offset between the aragonite components and siderite components is related to the differing equilibrium ^{18}O fractionations for siderite and aragonite, with both likely crystallizing from the waters of the same $\delta^{18}O$ compositions.

Endmember compositions and temperature used in mixing modeling are shown in Table 3. For water oxygen mixing calculations, a simple two-endmember linear mixing equation is used to calculate the $\delta^{18}O_w$ of mixtures. We assume DIC is dominated by HCO_3^-

and use the $\delta^{13}C_{HCO_3^-}$ calculated from the mineral $d^{13}C$ in all calculations. We use data reported for hydrogenotrophic methanogenic systems to estimate the DIC of the various water masses [68–70]. The $\delta^{13}C_{HCO_3^-}$ calculations include a mass balance for DIC, assuming a closed system and no loss or addition of CO_2. Mixing calculations for siderite–calcite water mixtures assumed constant temperature (17.57 °C). Mixing for siderite–river water mixtures uses a linear model with a siderite endmember temperature of 17.57 °C and river water endmember at 20.35 °C.

Table 3. Endmember compositions for mixing calculations. * River water with 1–3 endmembers covers the range of siderite–aragonite mixtures.

Endmember	t °C	$\delta^{18}O_w$	$\delta^{13}C_{HCO_3^-}$	DIC (mmol)
Siderite GW	17.57	−8.00	0.05	6.00
Calcite GW 1	17.57	−15.89	15.00	21.00
Calcite GW 2	17.57	−15.89	14.63	17.25
Calcite GW 3	17.57	−15.89	114.25	13.50
Calcite GW 4	17.57	−15.89	13.38	9.75
Calcite GW 5	17.57	−15.89	13.50	6.00
River water 1 *	20.35	−12.03	5.00	12.00
River water 2 *	20.35	−12.03	4.47	11.40
River water 3 *	20.35	−12.03	3.94	10.20
River water 4	20.35	−12.03	3.41	9.60
River water 5	20.35	−12.03	2.00	4.43

4.2. Fluid Mixing Processes

The siderite $\delta^{18}O$ and $\delta^{13}C$ trends suggest mixing between waters with distinct isotopic compositions. The scenarios for mixing siderite-forming groundwater with calcite-forming groundwater are simple. Because the calcite postdates siderite, it implies an evolution of the systems attributable to either early burial or the evolution of the aquifer downgradient. Although we assumed isothermal conditions in our mixing calculations, we cannot rule out different temperatures for the endmember calcite and siderite waters. Indeed, the average $\delta^{18}O_w$ of −10.16 °C calculated from the siderite data is significantly warmer than the −12.28 °C estimated using the paleolatitudinal relationship presented by [24]. However, the siderite water data could result from rainwater dilution, flooding that impacts the uppermost part of the aquifer during the rainy season, or simply river water entering the groundwater system via infiltration below the river channel. In addition, the siderite in the shallower part of the aquifer could be impacted by seasonal temperature changes.

The higher $\delta^{13}C$ values of the aragonite, and thus the calculated $\delta^{13}C_{HCO_3^-}$, are unlikely to have resulted from anaerobic methanogenesis within the river waters in which the mollusks lived. It is likely that CO_2 in equilibrium with the ^{13}C-enriched DIC either diffused upwards through the bottom sediment or groundwater entered the river where it was no longer siderite saturated or anaerobic. Because siderite fills molluscan interior shell pore spaces (and thus postdated the mollusk's mortality), the most likely scenario is that of ^{13}C-enriched CO_2 diffusing upward from underlying anaerobic methanogenic groundwaters during early burial and then infilling molluscan intraskeletal pore space with siderite cement in geopetal muds. Moreover, the mechanisms by which heavy $\delta^{13}C_{HCO_3^-}$ is delivered to the living gastropods is not conducive to mixing these waters with the siderite-precipitating groundwater.

4.3. Geochemcial Support for Freshwater in the Literature

The findings that form the core of this paper thus support the previous hypothesis test provided by Holmden et al. [20,21], which similarly interpreted only freshwater origins for McMurray sediments based on other geochemical proxies ($^{87}Sr/^{86}Sr$ and Sr/Ca) from well-preserved fossil material from gastropods, ammonites, composite shell material, and whole rock limestone from Alberta, Saskatchewan, and Montana. Sr-isotope data showed

evidence of mixing between fresh and brackish waters, yet the fossil material showed only evidence of the mixing of two distinct freshwaters, according to Holmden et al. [21].

Holmden et al. [20] only found evidence of freshwater during the deposition of the Ostracode Zone, a unit above the McMurray, which is interpreted to have been a large lake or lake system covering what is today multiple states/provinces being fed by the continental-scale river system implicated in depositing McMurray sediments. This lake was originally interpreted by Holmden et al. [20] to have had its oxygen isotopic composition controlled by the evaporation of riverine water to $\sim -10‰$. More recent work unraveling the paleo-meteorology of the region [22,24,71] interpreted humid conditions and a significant rainfall that would have limited any such evaporation, suggesting that the $-10‰$ value was more likely reflective of the high paleolatitude of the region during the Albian.

4.4. Local Paleogeographic Effects

Eastern paleovalley fills in the McMurray at this level do not show evidence of arc contributions, despite the arc's presence at this time (though this could also be explained by a lack of arc-derived zircons from a volcanic lull). The arc was subsequently a significant contributor during Clearwater and Grand Rapid deposition, and those units have abundant zircon grains from the McMurray time, suggesting that they were non-volcanogenic and needed to be exhumed first [9]. This discounts the hypothesis of orographic effects explaining the low $\delta^{18}O$ values observed in this study and leads directly to the alternative, catchment effects hypothesis from a continental-scale river system.

5. Conclusions

From the isotopic data presented herein, gastropods collected from the Upper McMurray Formation lived their life and were subject to early burial in an environment where waters were of terrestrial (i.e., fresh, meteoric) origin.

- Siderite is a common hallmark of diagenesis in terrestrial ecosystems [72–76].
- Calculated paleo-water $\delta^{18}O$ is consistent with terrestrial ecosystems rather than marine-influenced waters.
- The range of $\delta^{18}O$ values from gastropod shells and authigenic carbonate cement reported herein suggests that the Upper McMurray Formation was deposited by a continental-scale river system, producing so-called "catchment effects" on stable isotopic variability.

This study is limited to analyzing relatively few samples from a single geographic locality, though the detailed nature of the geochemical sampling often precludes expansive data collection in a single study. Future studies could apply this method to other areas of the McMurray to identify spatial variation in the extent of freshwater influence, perhaps identifying where brackish conditions begin. Indeed, it could also be expanded to other stratigraphic units in the Mannville Group to assess changes in the hydrology of those units.

The well-preserved carbonate material could also be analyzed for its temperature of formation via clumped isotope geochemistry, which, combined with traditional stable isotopes, could more quantitatively estimate the paleo-water $\delta^{18}O$, giving insights into the Cretaceous water cycle.

Conflicts of Interest: The authors declare no conflicts of interest.

References

1. Dusseault, M.B. Comparing Venezuelan and Canadian heavy oil and tar sands. In Proceedings of the Canadian International Petroleum Conference, Calgary, AB, Canada, 12–14 June 2001. PAPER 2001-061.
2. Alberta Energy Regulator, 2024, Maps, Map Viewers, and Shapefiles. Available online: https://www.aer.ca/providing-information/data-and-reports/maps-mapviewers-and-shapefiles (accessed on 26 February 2024).
3. Wightman, D.M.; Pemberton, S.G. *The Lower Cretaceous (Aptian) McMurray Formation: An Overview of the Fort McMurray Area, Northeastern, Alberta*; Pemberton, S.G., James, D.P., Eds.; Petroleum Geology of the Previous Cretaceous Mannville Group, Western Canada; Canadian Society of Petroleum Geologists Memoir 18; Canadian Society of Petroleum Geology: Calgary, AB, Canada, 1997; pp. 312–344.
4. Hubbard, S.M.; Smith, D.G.; Nielsen, H.; Leckie, D.A.; Fustic, M.; Spencer, R.J.; Bloom, L. Seismic geomorphology and sedimentology of a tidally influenced river deposit, Lower Cretaceous Athabasca oil sands, Alberta, Canada. *AAPG Bull.* **2011**, *95*, 1123–1145. [CrossRef]
5. Labrecque, P.A.; Jensen, J.L.; Hubbard, S.M.; Nielsen, H. Sedimentology and stratigraphic architecture of a point bar deposit, Lower Cretaceous McMurray Formation, Alberta, Canada. *Bull. Can. Pet. Geol.* **2011**, *59*, 147–171. [CrossRef]
6. Fustic, M.; Hubbard, S.M.; Spencer, R.; Smith, D.G.; Leckie, D.A.; Bennett, B.; Larter, S. Recognition of down-valley translation in tidally influenced meandering fluvial deposits, Athabasca Oil Sands (Cretaceous), Alberta, Canada. *Mar. Pet. Geol.* **2012**, *29*, 219–232.
7. Moreton, D.J.; Carter, B.J. Characterizing alluvial architecture of point bars within the McMurray Formation, Alberta, Canada, for improved bitumen resource prediction and recovery. In *Developments in Sedimentology*; Elsevier: Amsterdam, The Netherlands, 2015; Volume 68, pp. 529–559.
8. Durkin, P.R.; Boyd, R.L.; Hubbard, S.M.; Shultz, A.W.; Blum, M.D. Three-dimensional reconstruction of mean-der-belt evolution, Cretaceous McMurray Formation, Alberta foreland basin, Canada. *J. Sediment. Res.* **2017**, *87*, 1075–1099. [CrossRef]
9. Blum, M.; Pecha, M. Mid-Cretaceous to Paleocene North American drainage reorganization from detrital zircons. *Geology* **2014**, *42*, 607–610. [CrossRef]
10. Benyon, C.; Leier, A.; Leckie, D.A.; Webb, A.; Hubbard, S.M.; Gehrels, G. Provenance of the Cretaceous Athabasca Oil Sands, Canada: Implications for Continental-Scale Sediment Transport. *J. Sediment. Res.* **2014**, *84*, 136–143. [CrossRef]
11. Benyon, C.; Leier, A.L.; Leckie, D.A.; Hubbard, S.M.; Gehrels, G.E. Sandstone provenance and insights into the paleogeography of the McMurray Formation from detrital zircon geochronology, Athabasca Oil Sands, Canada. *AAPG Bull.* **2016**, *100*, 269–287. [CrossRef]
12. Wahbi, A.M.; Blum, M.D.; Doerger, C.N. Early Cretaceous continental-scale sediment routing, the McMurray Formation, Western Canada Sedimentary Basin, Alberta, Canada. *GSA Bull.* **2022**, *135*, 2088–2106. [CrossRef]
13. Blum, M. The McMurray conundrum. *Reservoir* **2017**, *2*, 25–29.
14. Gingras, M.K.; Leckie, D.A. The argument for tidal and brackish water influence in the McMurray Formation reservoirs. *Reservoir* **2017**, *2*, 21–24.
15. Blum, M.; Martin, J.; Milliken, K.; Garvin, M. Paleovalley systems: Insights from Quaternary analogs and experiments. *Earth-Sci. Rev.* **2013**, *116*, 128–169. [CrossRef]
16. Fernandes, A.M.; Törnqvist, T.E.; Straub, K.M.; Mohrig, D. Connecting the backwater hydraulics of coastal rivers to fluvio-deltaic sedimentology and stratigraphy. *Geology* **2016**, *44*, 979–982. [CrossRef]
17. Allan, J.R.; Matthews, R.K. Carbon and oxygen isotopes as diagenetic and stratigraphic tools: Surface and subsurface data, Barbados, West Indies. *Geology* **1977**, *5*, 16–20. [CrossRef]
18. Meyers, W.J.; Lohmann, K.C. *Isotope Geochemistry of Regionally Extensive Calcite Cement Zones and Marine Com-Ponents in Mississippian Limestones, New Mexico*; Carbonate Cements SEPM Special Publication 36; SEPM (Society for Sedimentary Geology): Tulsa, OK, USA, 1985.
19. Lohmann, K.C. Geochemical patterns of meteoric diagenetic systems and their application to studies of paleokarst. In *Paleokarst*; Springer: New York, NY, USA, 1988; pp. 58–80.
20. Holmden, C.; Creaser, R.; Muehlenbachs, K. Paleosalinities in ancient brackish water systems determined by 87Sr/86Sr ratios in carbonate fossils: A case study from the Western Canada sedimentary basin. *Geochim. Cosmochim. Acta* **1997**, *61*, 2105–2118. [CrossRef]

21. Holmden, C.; Muehlenbachs, K.; Creaser, R.A. *Depositional Environment of the Early Cretaceous Ostracode Zone: Paleohydrologic Constraints from O, C and Sr Isotopes. Petroleum Geology of the Cretaceous Mannville Group, Western Canada*; Pemberton, S.G., James, D.P., Eds.; Memoir 18; Canadian Society of Petroleum Geologists: Calgary, AB, Canada, 1997; pp. 77–92.

22. Ufnar, D.F.; Gonzalez, L.A.; Ludvigson, G.A.; Brenner, R.L.; Witzke, B.J. Stratigraphic implications of meteoric sphaerosiderite δ18O values in paleosols of the Cretaceous (Albian) Boulder Creek Formation, NE British Columbia foothills, Canada. *J. Sediment. Res.* **2001**, *71*, 1017–1028. [CrossRef]

23. Ufnar, D.F.; González, L.A.; Ludvigson, G.A.; Brenner, R.L.; Witzke, B.J. The mid-Cretaceous water bearer: Isotope mass balance quantification of the Albian hydrologic cycle. *Palaeogeogr. Palaeoclim. Palaeoecol.* **2002**, *188*, 51–71. [CrossRef]

24. Suarez, M.B.; González, L.A.; Ludvigson, G.A. Quantification of a greenhouse hydrologic cycle from equatorial to polar latitudes: The mid-Cretaceous water bearer revisited. *Palaeogeogr. Palaeoclim. Palaeoecol.* **2011**, *307*, 301–312. [CrossRef]

25. Ross, J.B.; Ludvigson, G.A.; Schröder-Adams, C.J.; Suarez, M.B. High latitude meteoric δ18O compositions from the Cenomanian Bastion Ridge Formation, Axel Heiberg Island, Canadian Arctic Archipelago: A palaeoclimate proxy from the Sverdrup Basin. *Geol. Soc. Lond. Spec. Publ.* **2020**, *498*, 57–74. [CrossRef]

26. DeCelles, P.G. Late Jurassic to Eocene evolution of the Cordilleran thrust belt and foreland basin system, western USA. *Am. J. Sci.* **2004**, *304*, 105–168. [CrossRef]

27. Miall, A.D.; Catuneanu, O.; Vakarelov, B.K.; Post, R. The Western interior basin. *Sediment. Basins World* **2008**, *5*, 329–362.

28. Wellner, R.W.; Varban, B.L.; Roca, X.; Flaum, J.A.; Stewart, E.K.; Blum, M.D. Simple is better when it comes to sequence stratigraphy: The Clearwater Formation of the Mannville Group reinterpreted using a genetic body approach. *AAPG Bull.* **2018**, *102*, 447–482. [CrossRef]

29. Alberta Energy and Utilities Board. *Athabasca Wabiskaw-McMurray Regional Geological Study*; Report 2003-A; Alberta Energy and Utilities Board: Calgary, AB, Canada, 2003.

30. Rinke-Hardekopf, L.; Dashtgard, S.; MacEachern, J. Earliest Cretaceous Transgression of North America Recorded in Thick Coals: McMurray Sub-Basin, Canada. *Int. J. Coal Geol.* **2019**, *204*, 18–33. [CrossRef]

31. Rinke-Hardekopf, L.; Dashtgard, S.E.; MacEachern, J.A.; Gingras, M.K. Resolving stratigraphic architecture and constraining ages of paralic strata in a low-accommodation setting, Firebag Tributary, McMurray Formation, Canada. *Depos. Rec.* **2022**, *8*, 754–785. [CrossRef]

32. Selby, D.; Creaser, R.A. Direct Radiometric Dating of Hydrocarbon Deposits Using Rhenium-Osmium Isotopes. *Science* **2005**, *308*, 1293–1295. [CrossRef] [PubMed]

33. Hein, F.J.; Dolby, G.; Fairgrieve, B. A Regional Geologic Framework for the Athabasca Oil Sands, Northeastern Alberta, Canada. In *Heavy-Oil and Oil-Sand Petroleum Systems in Alberta and Beyond*; Hein, F.J., Leckie, D., Larter, S., Suter, J.R., Eds.; AAPG Studies in Geology 64; American Association of Petroleum Geologists: Tulsa, OK, USA, 2012; pp. 207–250.

34. Barton; Porter, I.; O'byrne, C.; Mahood, R.; Cotterill, D. Impact of the Prairie Evaporite dissolution collapse on McMurray stratigraphy and depositional patterns, Shell Albian Sands Lease 13, northeast Alberta. *Bull. Can. Pet. Geol.* **2017**, *65*, 175–199. [CrossRef]

35. Broughton, P.L. Alignment of fluvio-tidal point bars in the middle McMurray Formation: Implications for structural architecture of the Lower Cretaceous Athabasca Oil Sands Deposit, northern Alberta. *Can. J. Earth Sci.* **2016**, *53*, 896–930. [CrossRef]

36. Sloss, L.L.; Merriam, D.F. Tectonic cycles of the North American craton. *Kans. Geol. Surv. Bull.* **1964**, *169*, 449–460.

37. Carrigy, M.A. *Geology of the McMurray Formation: Part III General Geology of the McMurray Area*; Memoir 1; Research Council of Alberta, Geological Division: Edmonton, AB, Canada, 1959; 130p.

38. Flach, P.D.; Mossop, G.D. Depositional environments of Lower Cretaceous McMurray Formation, Athabasca Oil Sands, Alberta. *AAPG Bull.* **1985**, *69*, 1195–1207.

39. Carrigy, M.A. Deltaic Sedimentation in Athabasca Tar Sands. *AAPG Bull.* **1971**, *55*, 1155–1169.

40. Nelson, H.W.; Glaister, R.P. Subsurface environmental facies and reservoir relationships of the McMurray oil sands, northeastern Alberta. *Bull. Can. Pet. Geol.* **1978**, *26*, 177–207.

41. Horner, S.C.; Hubbard, S.M.; Martin, H.K.; Hagstrom, C.A. Reconstructing basin-scale drainage dynamics with regional subsurface mapping and channel-bar scaling, Aptian, Western Canada Foreland Basin. *Sediment. Geol.* **2019**, *385*, 26–44. [CrossRef]

42. Smith, D.G. Tidal bundles and mud couplets in the McMurray Formation, northeastern Alberta, Canada. *Bull. Can. Pet. Geol.* **1988**, *36*, 216–219.

43. Russell, L.S. Mollusca from the McMurray Formation of northern Alberta. *Trans. R. Soc. Can. Sect.* **1932**, *4*, 37–43.

44. Mellon, G.B.; Wall, J.H. Foraminifera of the upper McMurray and basal Clearwater formations. *Alta. Res. Counc. Rep.* **1956**, *72*, 1–29.

45. Pemberton, S.G.; Flach, P.D.; Mossop, G.D. Trace Fossils from the Athabasca Oil Sands, Alberta, Canada. *Science* **1982**, *217*, 825–827. [CrossRef] [PubMed]

46. Suarez, C.A.; Frucci, M.N.; Tompkins, T.B.; Suarez, M.B. Quantification of a North American greenhouse hydrological cycle: Using oxygen isotopic composition of phosphate from Early Cretaceous (Aptian–Albian) turtles. *Geol. Soc. Lond. Spec. Publ.* **2021**, *507*, 335–345. [CrossRef]

47. Friedman, I.; O'Neil, J.R. *Compilation of Stable Isotope Fractionation Factors of Geochemical Interest*; US Government Printing Office: Washington, DC, USA, 1977; Volume 440.

48. van Dijk, J.; Fernandez, A.; Müller, I.A.; Lever, M.; Bernasconi, S.M. Oxygen isotope fractionation in the sider-ite-water system between 8.5 and 62 °C. *Geochim. Cosmochim. Acta* **2018**, *220*, 535–551. [CrossRef]

49. Kohn, M.J.; Dettman, D.L. Paleoaltimetry from Stable Isotope Compositions of Fossils. *Rev. Miner. Geochem.* **2007**, *66*, 119–154. [CrossRef]

50. Dettman, D.L.; Reische, A.K.; Lohmann, K.C. Controls on the stable isotope composition of seasonal growth bands in aragonitic fresh-water bivalves (unionidae). *Geochim. Cosmochim. Acta* **1999**, *63*, 1049–1057. [CrossRef]

51. Grossman, E.L.; Ku, T.L. Oxygen and carbon isotope fractionation in biogenic aragonite: Temperature effects. *Chem. Geol. Isot. Geosci. Sect.* **1986**, *59*, 59–74. [CrossRef]

52. Deines, P.; Langmuir, D.; Harmon, R.S. Stable carbon isotope ratios and the existence of a gas phase in the evolution of carbonate ground waters. *Geochim. Cosmochim. Acta* **1974**, *38*, 1147–1164. [CrossRef]

53. Carothers, W.W.; Adami, L.H.; Rosenbauer, R.J. Experimental oxygen isotope fractionation between siderite-water and phosphoric acid liberated CO_2-siderite. *Geochim. Cosmochim. Acta* **1988**, *52*, 2445–2450. [CrossRef]

54. Scholle, P.A.; Ulmer-Scholle, D.S. *A Color Guide to the Petrography of Carbonate Rocks: Grains, Textures, Porosity, Diagenesis*; Memoir 77; American Association of Petroleum Geologists: Tulsa, OK, USA, 2003; 474p, ISBN 0-89181-358-6.

55. Götte, T.; Richter, D.K. Quantitative aspects of Mn-activated cathodoluminescence of natural and synthetic aragonite. *Sedimentology* **2009**, *56*, 483–492. [CrossRef]

56. Barbin, V. Application of cathodoluminescence microscopy to recent and past biological materials: A decade of progress. *Miner. Pet.* **2013**, *107*, 353–362. [CrossRef]

57. Janiszewska, K.; Mazur, M.; Machalski, M.; Stolarski, J. From pristine aragonite to blocky calcite: Exceptional preservation and diagenesis of cephalopod nacre in porous Cretaceous limestones. *PLoS ONE* **2018**, *13*, e0208598. [CrossRef]

58. Mozley, P.S.; Carothers, W.W. Elemental and isotopic composition of siderite in the Kuparuk Formation, Alaska: Effect of microbial activity and water/sediment interaction on early pore-water chemistry. *J. Sediment. Petrol.* **1992**, *62*, 681–692.

59. Kozłowska, A.; Feldman-Olszewska, A.; Kuberska, M.; Maliszewska, A. Diagenesis and the Conditions of Deposition of the Middle Jurassic Siderite Rocks from the Northern Margin of the Holy Cross Mountains (Poland). *Minerals* **2021**, *11*, 1353. [CrossRef]

60. Paxton, S.T.; Szabo, J.O.; Ajdukiewicz, J.M.; Klimentidis, R.E. Construction of an intergranular volume compaction curve for evaluating and predicting compaction and porosity loss in rigid-grain sandstone reservoirs. *AAPG Bull.* **2002**, *86*, 2047–2067.

61. Boggs, S.; Krinsley, D. *Application of Cathodoluminescence Imaging to the Study of Sedimentary Rocks*; Cambridge University Press: New York, NY, USA, 2006.

62. Ufnar, D.F.; Ludvigson, G.A.; González, L.A.; Brenner, R.L.; Witzke, B.J. High latitude meteoric $\delta^{18}O$ compositions: Paleosol siderite in the middle Cretaceous Nanushuk Formation, North Slope, Alaska. *Geol. Soc. Am. Bull.* **2004**, *116*, 463–473. [CrossRef]

63. Suarez, C.A.; Ludvigson, G.A.; Gonzalez, L.A.; Fiorillo, A.R.; Flaig, P.P.; McCarthy, P.J. Use of multiple oxygen isotope proxies for elucidating Arctic Cretaceous palaeo-hydrology. *Geol. Soc. Lond. Spec. Publ.* **2013**, *382*, 185–202. [CrossRef]

64. González, L.A.; Lohmann, K.C. Carbon and oxygen isotopic composition of Holocene reefal carbonates. *Geology* **1985**, *13*, 811–814. [CrossRef]

65. Lohmann, K.C.; Walker, J.C. The $\delta^{18}O$ record of Phanerozoic abiotic marine calcite cements. *Geophys. Res. Lett.* **1989**, *16*, 319–322. [CrossRef]

66. Choquette, P.W.; James, N.P. *Marine Diagenesis*; McIlreath, I., Morrow, D., Eds.; Geoscience Canada: Ottawa, Canada, 1990; Volume 10.

67. Dutton, A.; Wilkinson, B.H.; Welker, J.M.; Bowen, G.J.; Lohmann, K.C. Spatial distribution and seasonal variation in $^{18}O/^{16}O$ of modern precipitation and river water across the conterminous USA. *Hydrol. Process.* **2005**, *19*, 4121–4146. [CrossRef]

68. Martens, C.S.; Albert, D.B.; Alperin, M.J. Stable isotope tracing of anaerobic methane oxidation in the gassy sediments of Eckernfoerde Bay, German Baltic Sea. *Am. J. Sci.* **1999**, *299*, 589. [CrossRef]

69. Aravena, R.; Harrison, S.; Barker, J.; Abercrombie, H.; Rudolph, D. Origin of methane in the Elk Valley coalfield, southeastern British Columbia, Canada. *Chem. Geol.* **2003**, *195*, 219–227. [CrossRef]

70. Thomas, M.A. *Chemical and Isotopic Characteristics of Methane in Groundwater of Ohio, 2016*; US Geological Survey Scientific Investigations Report 2018-5097; US Geological Survey Scientific Investigations: Reston, VA, USA, 2018; 52p.

71. Ufnar, D.F.; Gonzalez, L.A.; Ludvigson, G.A.; Brenner, R.L.; Witzke, B.J.; Leckie, D. Reconstructing a Mid-Cretaceous Landscape from Paleosols in Western Canada. *J. Sediment. Res.* **2005**, *75*, 984–996. [CrossRef]

72. Ludvigson, G.A.; González, L.A.; Fowle, D.A.; Roberts, J.A.; Driese, S.G.; Villarreal, M.A.; Smith, J.J.; Suarez, M.B.; Nordt, L.C. *Paleoclimatic Applications and Modern Process Studies of Pedogenic Siderite*; New Frontiers in Paleopedology and Terrestrial Paleoclimatology; SEPM (Society for Sedimentary Geology): Tulsa, OK, USA, 2013.

73. Ludvigson, G.A.; González, L.A.; Metzger, R.A.; Witzke, B.J.; Brenner, R.L.; Murillo, A.P.; White, T.S. Meteoric sphaerosiderite lines and their use for paleohydrology and paleoclimatology. *Geology* **1998**, *26*, 1039–1042. [CrossRef]

74. Pickering, M.D.; Ghislandi, S.; Usai, M.R.; Wilson, C.; Connelly, P.; Brothwell, D.R.; Keely, B.J. Signatures of degraded body tissues and environmental conditions in grave soils from a Roman and an Anglo-Scandinavian age burial from Hungate, York. *J. Archaeol. Sci.* **2018**, *99*, 87–98. [CrossRef]

75. Bojanowski, M.J.; Goryl, M.; Kremer, B.; Marciniak-Maliszewska, B.; Marynowski, L.; Środoń, J. Pedogenic siderites fossilizing Ediacaran soil microorganisms on the Baltica paleocontinent. *Geology* **2020**, *48*, 62–66. [CrossRef]
76. Sengupta, R.; Robinson, S.A.; Tosca, N.J. Sphaerosiderites as sensitive recorders of non-marine depositional and diagenetic history: Insights from the Lower Cretaceous Wealden Supergroup. *Depos. Rec.* **2021**, *7*, 520–540. [CrossRef]